Calculating and communicating ensemble-based volcanic ash dosage and concentration risk for aviation

Article

Accepted Version

www.reading.ac.uk/centaur

CentAUR

Central Archive at the University of Reading

Reading's research outputs online

1

Calculating and communicating ensemble-based volcanic ash dosage and concentration risk for aviation

Andrew T. Prata,[a]* Helen F. Dacre,[a] Emma A. Irvine,[a] Eric Mathieu,[a] Keith P. Shine[a] and

Rory J. Clarkson[b]

[a]*Department of Meteorology, University of Reading, UK*

[b]*Engine Environmental Protection, Rolls-Royce plc, Derby, UK*

ABSTRACT: During volcanic eruptions, aviation stakeholders require an assessment of the volcanic ash hazard. Operators and regulators are required to make fast decisions based on deterministic forecasts, which are subject to various sources of uncertainty. For a robust decision to be made, a measure of the uncertainty of the hazard should be considered but this can lead to added complexity preventing fast decision making. Here a proof-of-concept risk matrix approach is presented that combines uncertainty estimation and volcanic ash hazard forecasting into a simple warning system for aviation. To demonstrate the methodology, an ensemble of 600 dispersion model simulations is used to characterise uncertainty (due to eruption source parameters, meteorology and internal model parameters) in ash dosages and concentrations for a hypothetical Icelandic eruption. To simulate aircraft encounters with volcanic ash, trans-Atlantic air routes between New York (JFK) and London (LHR) are generated using time-optimal routing software. This approach has been developed in collaboration with operators, regulators and engine manufacturers; it demonstrates how an assessment of ash dosage and concentration risk

23 can be used to make fast and robust flight-planning decisions even when the model uncertainty

24 spans several orders of magnitude. The results highlight the benefit of using an ensemble over a

25 deterministic forecast and a new method for visualising dosage risk along flight paths. The risk

26 matrix approach is applicable to other aviation hazards such as SO_2 dosages, desert dust, aircraft

27 icing and clear-air turbulence and is expected to aid flight-planning decisions by improving the

28 communication of ensemble-based forecasts to aviation.

29

32

1. Introduction

34 Flight-planning decisions during volcanic eruptions pose many challenges to the aviation

35 industry. An important issue in the decision-making process is the economic impact of grounding

36 and re-routing aircraft during an eruption event and the potential for damage to the engines due

37 to flying in ash clouds at low concentration levels that do not cause an immediate safety risk.

38 While aircraft encounters with volcanic ash are a known safety issue (Casadevall, 1994; Prata

39 and Tupper, 2009; Guffanti and Tupper, 2015), there have been many incidents which suggest

40 that aircraft engines can tolerate low concentrations of ash without catastrophic engine failure. A

41 total of 131 incidents were reported between 1953–2009 and a further 122 were documented for

42 the period from 2010–2016 (Guffanti *et al.*, 2010; Christmann *et al.*, 2017). The increase in

43 documented aircraft encounters between 2010–2016 may be partly a result of better reporting

44 and the publicity of the 2010 Eyjafjallajökull eruption in Iceland. However, as the number of

45 aircraft flying in volcanically active regions around the globe continues to grow—Airbus

46 projects a doubling of passenger aircraft from 2017–2036 (Airbus, 2017)—the number of aircraft

47 encounters with volcanic ash and gas clouds are likely to increase with the potential to lead to

48 serious global economic impacts. In this paper a new way of calculating and communicating

49 volcanic ash forecasts which allows the aviation community to assess the risks associated with

50 flying along a given route and to make flight-planning decisions is presented.

51 The eruptions of Eyjafjallajökull (Iceland) in April and May 2010 had a profound economic

52 impact on the aviation industry. So much so that it prompted changes to the approach taken by

53 regulators towards flying in ash-contaminated airspace. At the time, the International Civil

54 Aviation Organization (ICAO) recommended that all encounters with volcanic ash clouds should

55 be avoided, regardless of the ash concentration (ICAO, 2007). This approach became

56   unworkable during the crisis which put pressure on regulators to re-open controlled airspace

57   where ash concentrations were forecast to be low. In response, the UK Civil Aviation Authority

58   (CAA) in consultation with Rolls-Royce, the UK Met Office, international and European

59   regulators and aviation experts developed quantitative peak concentration limits (Witham *et al.*,

60   2012; Clarkson *et al.*, 2016). Currently, the ICAO EUR/NAT (European and North Atlantic)

61   Volcanic Ash Contingency Plan uses peak concentration limits to define low (≤ 2 mg m^{-3}),

62   medium (2–4 mg m^{-3}) and high (≥ 4 mg m^{-3}) ash contamination levels (ICAO, 2016). The

63   European Aviation Safety Agency (EASA) and UK CAA have adopted these ash contamination

64   levels and operators are required to have a Safety Risk Assessment approved by their National

65   Aviation Authority before considering entering airspace forecast to contain medium or high ash

66   contamination levels (CAA, 2017).

67   The UK Met Office and Météo-France currently provide quantitative peak concentration

68   forecasts (defined in Section 2) as supplementary information to Volcanic Ash Advisories and

69   Volcanic Ash Graphics issued by the London and Toulouse Volcanic Ash Advisory Centres

70   (VAACs), respectively. Peak concentrations, however, do not take into consideration the

71   situations where an aircraft may be flying through a low concentration ash cloud for a long

72   period of time, which may lead to engine damage (Wylie *et al.*, 2017), or a moderate

73   concentration for a relatively short period of time, which may not lead to engine damage.

74   Volcanic ash dosages represent the accumulated concentration over time along an aircraft's

75   route, thus accounting for the situations above.

76   Recently, Rolls-Royce announced an ash dosage threshold below which exposures will not

77   lead to significant reductions in flight safety margins (Rolls-Royce, 2017). Up to ash

78   concentrations of 4 mg m^{-3} the threshold has been set at a dosage of 14.4 g m^{-3} s. This value was

79   calculated based on the assessment that a Rolls-Royce engine should be able to maintain all

80   safety margins after spending 1 h in a concentration of 4 mg m^{-3} or 2 h in a concentration of 2

81   mg m^{-3}. As a result of limitations set by EASA the appropriate dosage above 4 mg m^{-3} has not

82   been defined. These recent developments motivate the need to develop a framework that

83   combines quantitative ash concentration forecasts with air route data to quantify ash dosages

84   along flight paths and their uncertainties.

85   The move to quantitative ash concentration limits has driven rapid development and

86   improvement in volcanic ash concentration forecasting (e.g. Stohl *et al.*, 2011; Dacre *et al.*,

87   2011; Devenish *et al.*, 2012; Millington *et al.*, 2012; Webster *et al.*, 2012). However, dispersion

88   model simulations are subject to various sources of uncertainty which are currently not taken

89   account of by operational deterministic forecasts. Communicating this uncertainty to aviation

90   stakeholders is of prime importance as this information can be used to make better-informed

91   decisions (Mulder *et al.*, 2017).

92   The major sources of uncertainty in volcanic ash transport and dispersion models include

93   uncertainty in the eruption source parameters (e.g. mass eruption rate and plume height), internal

94   model parameterisations (e.g. wet deposition and free tropospheric turbulent mixing) and the

95   driving meteorology (Folch, 2012; Harvey *et al.*, 2018). The challenge is then to develop a

96   robust methodology which accounts for these uncertainties objectively, but also allows for fast

97   decisions to be made by operators and regulators. Robust decisions from quantitative data require

98   a measure of their uncertainties. A common method for representing uncertainty in weather

99   forecasting is to develop an ensemble: a set of model realisations created by perturbing various

100   uncertain parameters used at the start of each model run (e.g. Palmer, 2002; Buizza *et al.*, 2005;

101   Gneiting and Raftery, 2005). An ensemble (probabilistic) forecast allows for a robust decision as

102 it can be used to quantify the likelihood of a certain event occurring. It is therefore logical to

103 extend ensemble forecasting methods to dispersion modelling of volcanic ash concentrations. An

104 example in the context of the ash–aviation problem would be the likelihood of the ash

105 concentration being above a certain threshold. However, too much (or too complex) information

106 can prevent a decision-maker from making a fast decision, which is generally a requirement in

107 operational settings. This issue is often referred to as 'information overload' and was raised as a

108 major concern by operators and regulators during and following the 2010 Eyjafjallajökull crisis.

109 The UK Met Office National Severe Weather Warning Service utilises the concept of a risk

110 matrix to communicate ensemble-based forecasts of severe weather events to the public (Neal *et*

111 *al.*, 2014). *Risk* is defined as the product of the *likelihood* and *impact* of an event occurring. A

112 risk matrix is constructed by discretising likelihoods and impacts into different ranges and

113 assigning a risk severity to each combination of the impact and likelihood ranges. This approach

114 addresses the issue of information overload by condensing probabilistic information into

115 appropriate courses of action to be taken by the relevant stakeholders (e.g. the public, an airline

116 operator, emergency services etc.). In the present study, this approach is adapted to the ash–

117 aviation problem by considering ash dosage and peak concentration as *impact* and using

118 ensemble modelling to quantify their *likelihood*.

119 The aim of this paper is to develop a proof-of-concept methodology for implementing a risk-

120 based approach to flight planning; using ash dosage and concentration encountered by an aircraft

121 along its flight path (hereafter known as 'along-route ash dosage and/or concentration'). To

122 generate ash concentration data, a hypothetical Icelandic eruption scenario resulting in ash

123 dispersal across the North Atlantic was simulated using the dispersion model used operationally

124 by the London VAAC (LVAAC). Trans-Atlantic air routes were generated using time-optimal

125   routing software to simulate ash encounters permitting ash dosage calculations. An ensemble

126   dataset was developed (based on uncertainty in the meteorology, eruption source parameters and

127   internal model parameterisations) to estimate the likelihood of certain ash dosage and peak

128   concentration ranges. The ash dosage risk was then calculated for various flight routes to

129   demonstrate how airline operators might use this information.

2. NAME model setup

131   The Numerical Atmospheric-dispersion Modelling Environment (NAME; Jones *et al.*, 2007) is a

132   Lagrangian dispersion model used operationally by the LVAAC. The Lagrangian representation

133   of atmospheric dispersion within NAME allows for each model particle to be tracked as it is

134   advected by the three-dimensional wind fields. If the size (volume), shape and density of a

135   particle are known its mass can be calculated. Mass concentration fields are calculated in NAME

136   by dividing the total mass of particles in a given grid box by its volume.

137   In the present study, NAME (version 6.5) was used to simulate a hypothetical Icelandic

138   eruption using the default setup of the LVAAC. Ash (mass) concentrations were output onto a

139   global grid of 800 by 600, corresponding to a grid resolution of approximately 0.451 ° longitude

140   by 0.301 ° latitude (~40 km horizontal resolution), at 22 flight levels (FL) from FL000 to FL550

141   (1013.25 to 91.15 hPa) with a vertical resolution of 25FL. Note that flight levels are defined as

142   standardised pressure altitudes expressed in units of hundreds of feet and are based on the ICAO

143   standard atmosphere. The concentration fields were output every 6 h using a 6 h time average

144   with a total run time of 66 h. The eruption plume was defined as a uniformly distributed vertical

145   line source extending from the volcano summit to the eruption plume height and the particle

146   release rate was set to 15000 h^{-1}, which is consistent with the model set up at the LVAAC

147   (Witham *et al.*, 2016). Finally, to convert to peak concentrations, the mean ash concentration

148   fields output by NAME were multiplied by a factor of 10. This is known as the 'peak-to-mean'

149   factor and has been adopted by the LVAAC to account for peak concentrations that cannot be

150   resolved by the NAME model (Webster *et al.*, 2012). This model configuration is referred to as

151   the 'thin layer' setup hereafter and is equivalent to the '25FL layer scheme' described in Webster

152   *et al.* (2012). The output from the thin layer setup in NAME was then post-processed to produce

153   the LVAAC's 'thick layer' product. The 'thick layer' product was produced by dividing the

154   vertical grid into three flight level ranges (FL000–FL200, FL200–FL350 and FL350–FL550) and

155   then setting the maximum ash concentration of the thin layers (25FL thickness) within each

156   range to the concentration of each thick layer (Figure 1).

157   2.1.   Meteorological data

158   The meteorological data that were used to drive NAME includes two datasets: an analysis dataset

159   produced by the Met Office Unified Model (MetUM; Cullen, 1993; Brown *et al.*, 2012) and an

160   ensemble dataset produced using the European Centre for Medium-Range Weather Forecasts

161   (ECMWF) Integrated Forecast System (IFS) (Buizza *et al.*, 1999). The MetUM analysis fields

162   have a horizontal resolution of ~17 km and vertical resolution of ~0.7 km in the upper

163   troposphere/lower stratosphere (UTLS). The time resolution of the MetUM data is 3 hourly

164   alternating from analysis to forecast fields every 3 h. At time intervals smaller than 3 h, the

165   meteorology fields are linearly interpolated. The MetUM dataset was used to drive NAME for

166   the control run (described in Section 2.2). The ECMWF IFS (cycle 43r1) was used to create an

167   ensemble of forecast meteorology. These data were archived at a horizontal resolution of 16 km

168   (T1279 spectral truncation) and vertical resolution of ~1.4 km in the UTLS with a time

169   resolution of 3 h and forecast lead-time of 66 h. These data were then extracted onto a regular

170   latitude/longitude grid of 0.125 ° by 0.125 ° and the precipitation, surface stresses and sensible

171   heat flux fields were post-processed so that they could be read in by NAME. To account for

172   uncertainty in the initial meteorological fields, the ECMWF IFS Ensemble Prediction System

173   (EPS) was used to produce a 20-member meteorological ensemble. The EPS utilises the singular-

174   vector approach (Buizza and Palmer, 1995) to perturb initial conditions in the meteorology and a

175   stochastic physics scheme (Buizza *et al.*, 1999) to account for model uncertainty. The ECMWF

176   dataset was used to investigate four sources of uncertainty in dispersion modelling: eruption

177   source parameters, internal NAME model parameters, initial meteorological conditions and error

178   growth with increasing forecast lead-time.

179   2.2.   Icelandic eruption scenario

180   The parameters used to define an eruption in NAME are referred to as eruption source

181   parameters (ESPs). These include the timing, location, duration, plume height, geometry and

182   vertical ash distribution of each eruptive phase during an event as well as the mass eruption rate

183   (MER) and microphysical properties of the distal fine ash particles (shape, density and size

184   distribution). In the following, the control run ESPs for the Icelandic eruption scenario are

185   described.

186   An explosive eruption from an Icelandic volcano has the potential to release volcanic ash at

187   aircraft cruising altitudes. Depending on the weather conditions, this type of eruption could result

188   in widespread ash dispersal across the North Atlantic and neighbouring landmasses, disrupting

189   trans-Atlantic air-traffic. The Katla volcano (19.083 ° W, 63.633 ° N, 1490 m a.s.l.) was selected

190   for the eruption scenario as it is an active volcano in Iceland with the potential for an explosive

191   ash-rich eruption. The eruption plume height was set to 15 km a.s.l. with a duration of 16 h to

192   ensure significant ash dispersal at cruise altitude (~10 km). Following the current approach of the

193   LVAAC, the MER was calculated from the plume height using the empirically-derived Mastin *et*

194   *al.* (2009) relationship. As the total grain size distribution is not modelled in NAME, the fraction

195   of mass due to fine ash (diameters ≤ 100 µm) must be considered. This is known as the distal

196   fine ash fraction (DFAF) and is also included as an ESP here. As the DFAF is the percentage of

197   mass assumed to remain in the atmosphere after an initial eruption, the MER is scaled by this

198   percentage. A DFAF of 5% was chosen as this is the default value used by the LVAAC for an

199   Icelandic eruption (Witham *et al.*, 2016). Similarly, the LVAAC's default ash size distribution

200   was used (see Witham *et al.*, 2016 Table 1) and the shape of the particles were assumed to be

201   spherical.

202   The eruption start time was set to 1 January 2017 at 0300 UTC as during this time an upper-

203   level ridge had formed over Iceland and the North Atlantic Ocean. This winter-time weather

204   regime is representative of the W3 and W4 categories identified by Irvine *et al.* (2013) as

205   frequent modes of variability in the North Atlantic. This meteorological situation occurs one

206   third of the time during the winter months and is characterised by northerly flow from Iceland

207   and persistent anticyclonic flow over the North Atlantic. In this scenario, volcanic ash from an

208   Icelandic eruption is dispersed toward the south and circulated over the North Atlantic for

209   several days. Due to large scale subsidence there is very little precipitation in this scenario and so

210   the amount of wet deposition is expected to be small. The control run ESPs are summarised in

211   Table 1 and the evolution of the ash cloud over 66 h in the control run simulation for the thick

212   layer concentrations from FL350–FL550 is shown in Figure 2.

213   **3. Ensemble simulations**

214   There are many ways to represent uncertainty in model simulations. In this paper, an ensemble of

215   NAME simulations is created by varying the meteorology, ESPs and internal model parameters.

216   Latin Hypercube Sampling (LHS; Iman and Conover, 1980) is a statistical technique that can be

217   used to efficiently generate an ensemble which ensures orthogonality between input model

218   parameter sets. The LHS method was used to generate a Latin Hypercube with 9 dimensions (i.e.

219   9 dispersion model input parameters were varied) and was sampled 600 times resulting in an

220   ensemble of 600 members. These simulations were conducted on the JASMIN 'super-data-

221   cluster' (Lawrence *et al.*, 2012) and took less than 1 h to complete for a 24-h ensemble forecast.

222   This runtime (and ensemble size) potentially allows an operational VAAC to provide 24 h

223   ensemble forecasts every 6 h; provided that they have sufficient computer resources and an

224   operational meteorological ensemble prediction system set up. All model parameters considered

225   in the LHS analysis were sampled from a uniform distribution. By sampling from a uniform

226   distribution, it is assumed that all values between their specified ranges are equally likely. The 9

227   model parameter choices (and their specified ranges) are listed in Table 1 and are described in

228   the following sections.

229   3.1.   Meteorological initial conditions and forecast error growth

230   It has been demonstrated that even for short lead-time forecasts (< 72 h) small differences in the

231   forecast wind fields can lead to large spread in the forecast ash clouds (Dacre and Harvey, 2018).

232   As described in Section 2.1, uncertainty in the initial meteorological fields as well as error

233   growth in the forecast fields were represented using the ECWMF dataset. These data make up a

234   20-member ensemble of meteorology. For the LHS sampling, ECMWF members were sampled

235   from a uniform distribution between 0 and 19. The random variable sampled from this range was

236   then rounded to the nearest integer. This index was then used to select (at random) an ECMWF

237   ensemble member for each of the 600 parameter sets.

238   3.2.   Eruption source parameters

239 To represent the uncertainty associated with the ESPs, a range of uncertainty (i.e. maximum and

240 minimum values) was assigned to each control run ESP and then randomly sampled from a

241 uniform distribution between the specified ranges (Table 1). The plume height, DFAF and MER

242 were selected for the LHS analysis as output from NAME has been shown to be the most

243 sensitive to these parameters (e.g. Dacre *et al.*, 2011; 2013; Harvey *et al.*, 2018). The source

244 timing (i.e. eruption onset) and duration were chosen to illustrate how uncertainty in these

245 parameters can lead to uncertainty in the timing and location of the modelled ash cloud.

246   The ranges selected for each ESP were made based on typical ranges reported in the

247 literature (e.g. Mastin *et al.*, 2009; Devenish *et al.*, 2012; Dacre *et al.*, 2013; Harvey *et al.*, 2018).

248 It is acknowledged that there is a degree of subjectivity in these choices; however, their specific

249 values do not alter the methodology developed to implement a risk-based approach (described in

250 Section 6) that can be used for making robust and fast flight-planning decisions.

251 3.3.   Internal model parameters

252 Dacre *et al.* (2015) have shown that the internal model parameters used in NAME to represent

253 free tropospheric turbulence can significantly impact the vertical depth (thickness) of volcanic

254 ash clouds and hence peak concentrations. These internal model parameters were also

255 investigated by Harvey *et al.* (2018) and were demonstrated to be the largest internal model

256 parameter contribution to uncertainty in NAME output. To represent uncertainty in free

257 tropospheric turbulence, the standard deviation (σ) and Lagrangian timescales (τ) of the

258 horizontal and vertical velocity components were sampled from a uniform distribution using the

259 range specified in Harvey *et al.* (2018). The horizontal and vertical components of these

260 parameters were varied in proportion to each other so that the shape of the turbulent eddies

261 parameterised in NAME is preserved. It is also noted that the horizontal component of standard

262   deviation of the free tropospheric turbulence was sampled on a logarithmic scale. Finally, the

263   standard deviation of the horizontal velocity for unresolved mesoscale motions was also sampled

264   from a uniform distribution following the ranges used in Harvey *et al.* (2018).

265   **4. Along-flight ash dosage**

266   To simulate aircraft encounters with volcanic ash, flight routes were generated using time-

267   optimal routing software developed by Irvine *et al.* (2016), which was based on the methodology

268   of Lunnon and Marklow (1992). The 'flightCode' program uses latitude and longitude pairs

269   representing the origin and destination airports for a given route, the constant true airspeed of the

270   aircraft and horizontal wind data at a given flight level. The code assumes that the aircraft is at a

271   fixed altitude and so take-off and landing are not considered. The output of flightCode is a set of

272   waypoints (latitude and longitude pairs) representing the fastest (time-optimal) route for the

273   specified airport pairs at a given instance in time given the prevailing wind at a given altitude.

274   In the present analysis, trans-Atlantic flights were generated assuming a constant true

275   airspeed of 250 m s^{-1} (900 km h^{-1}) and the MetUM dataset was used to provide horizontal wind

276   data at FL350 (assumed to be the cruise altitude of the aircraft). The eastbound and westbound

277   time-optimal routes from New York (JFK) to London (LHR) were calculated for each time step

278   of the dispersion model output (i.e. at 6 h intervals for 11 time steps).

279   The along-flight ash dosage is defined as the ash concentration multiplied by the time spent

280   in that concentration (duration of exposure) along an aircraft's flight path, which means that the

281   dosage, D, is expressed in units of grams per cubic metre seconds (g m^{-3} s):

$$D = \sum_{i=1}^{n} C_i \Delta t_i = \sum_{i=1}^{n} C_i \frac{\Delta s_i}{V_a} \qquad (1)$$

where n is the number of dispersion model grid boxes intersected by the air route, Δt_i is the

duration of exposure in the ith grid box, C_i is the ash concentration of the ith grid box

intersected, Δs_i is the distance travelled through the ith grid box and V_a is the true airspeed of the

aircraft. This definition means that dosage always increases monotonically along the route and is

distinct from Peterson and Dean (2007) who use 'ash exposure' (g m^{-2}) to quantify the potential

damage to aircraft intersecting ash clouds and Prata and Prata (2012) who defined dosage as the

accumulated mass of ash (g) along an aircraft's route. The definition adopted here (g m^{-3} s) is

consistent with the definitions used in Kristiansen *et al.* (2015), Clarkson *et al.* (2016), Wylie *et al.* (2017) and Prata *et al.* (2018); however, Clarkson *et al.* (2016) refer to dosage as a 'dose' in

their paper. All dosage calculations reported here assume that the modelled ash concentration

fields at a given time step are static (i.e. do not change with time) as the aircraft flies from the

origin to destination at its true airspeed. Note also that these ash concentrations correspond to the

post-processed ash concentrations at the FL350–FL550 thick layer level (described in Section 2)

and may result in overestimates of the along-route dosage at FL350 due to the application of the

peak-to-mean ratio and the approach of taking the maximum concentration of the thin layers

between FL350 and FL550 when determining the 'thick layer' concentration.

5. Representation of uncertainty

5.1.   Model agreement maps

The ensemble simulations (described in Section 3) were used to calculate the likelihoods of ash

concentrations exceeding different thresholds, based on output from NAME. Specifically, the

302   likelihoods represent the percentage of ensemble members that predicted an ash concentration

303   above a certain peak concentration threshold. Based on discussions with regulators and operators

304   these likelihoods were split into three ranges: less likely (0–10%), likely (10–90%) and very

305   likely (90–100%). It is noted that while regulators and operators suggested a three-category

306   system, the actual values of these boundaries were chosen by the authors to illustrate the present

307   method. In an operational setting, these values may be altered by the user to reflect their risk

308   appetite. Given that these percentages represent the level of agreement between ensemble

309   members these maps are referred to hereafter as 'model agreement maps' and do not strictly

310   constitute likelihoods. For ensemble simulations to represent true likelihoods they should be

311   calibrated using past observations and forecasts. However, in order to illustrate the proof-of-

312   concept risk matrix method in this paper, uncalibrated 'model agreement' values are used to

313   represent 'likelihoods' (described in Section 6). The likelihood boundaries represented on the

314   model agreement maps, however, depend on the ash concentration threshold chosen. The choice

315   of threshold was raised in meetings with various aviation stakeholders and thresholds ranging

316   from 0.2–10 mg m^{-3} were suggested.

317   To demonstrate how model agreement maps depend on ash concentration thresholds, four

318   model agreement maps (for FL350–FL550 at T+30) were generated; corresponding to four ash

319   concentration thresholds: 0.2, 2, 4 and 10 mg m^{-3}. Figures 3(a)–(d) show both the horizontal and

320   vertical model agreement maps for each of the peak concentration thresholds analysed. Note that

321   the vertical cross-sections were constructed by first calculating the time-optimal route at FL350

322   from JFK to LHR (return) and then calculating the ash concentration along this route for each

323   thick layer level. The ash concentration contours corresponding to each peak concentration

324   threshold from the control run are also overlaid on Figures 3(a)–(d) to demonstrate where an ash

325   cloud boundary might be drawn for a single (deterministic) forecast.

326   The horizontal model agreement maps reveal regions where there is high confidence in the

327   location of the ash cloud and concentration and regions where there is low model confidence.

328   Figure 3(a) shows the 0.2 mg m^{-3} ash concentration contour for the control run, which may be

329   used to determine the extent of a modelled ash cloud (Witham *et al.*, 2012). The model

330   agreement map indicates that over the western part of the British Isles a considerable percentage

331   (>10%) of ensemble member simulations contained ash above 0.2 mg m^{-3} whereas the control

332   simulation (black line) did not. This result demonstrates that, for this scenario, a single

333   (deterministic) model simulation would not have forecast ash concentrations above 0.2 mg m^{-3}

334   over this region while the ensemble, which accounts for uncertainty in the deterministic

335   simulation, shows that ash over this region was 'likely' (10–90%). Comparison of the different

336   ash concentration thresholds demonstrates that when the threshold is increased the region of

337   uncertainty increases relative to the control run (deterministic forecast). This is illustrated by

338   Figure 3(d) where the control run contour of 10 mg m^{-3} covers a small region over the middle

339   section of the westbound flight path and the ensemble indicates that ash concentrations above 10

340   mg m^{-3} are 'likely' (10–90%) over a larger region of the North Atlantic. The region of

341   uncertainty relative to the control run also increases with increasing ash concentration threshold

342   for the vertical model agreement maps, where this approach quantitatively shows the degree of

343   confidence in the model for ash concentrations at the three thick layer regions. In the bottom

344   panel of Figure 3(a), at approximately 5000 km along the route, the control run simulation

345   indicates ash at low altitudes; however, the model agreement contours indicate that > 10% of the

346   ensemble members resulted in ash concentrations above 0.2 mg m^{-3} at cruise altitude (FL350–

347   FL550 thick layer level).

348   In general, the area covered by each likelihood category was reduced as the ash concentration

349   threshold was increased (compare Figures 3(a)–(d)); however, the uncertain region over the

350   western part of the British Isles remained largely the same for thresholds up to 10 mg m^{-3}

351   (Figures 3(a)–(d)). This indicates that 10–90% of the ensemble members forecast ash

352   concentrations above 10 mg m^{-3} over this region (Figure 3(d)).

353   5.2.   Model agreement along routes

354   The ensemble approach can also be used to represent the uncertainty in ash dosage calculations.

355   However, as the dosage is calculated along a flight path, the model agreement values are

356   displayed as the percentage of ensemble members that predict the dosage to be above a certain

357   dosage threshold along the air route. Figure 4(a) shows the model agreement along the route

358   from JFK–LHR (return) at FL350–FL550 and T+30 using the Rolls-Royce airworthiness

359   threshold of 14.4 g m^{-3} s. When the model agreement is calculated along the route, the likelihood

360   of the aircraft engine exceeding the dosage threshold increases along the route. For comparison,

361   Figure 4(b) shows the same model agreement along the route but for a doubling of the dosage

362   threshold (i.e. 28.8 g m^{-3} s). As with the ash concentration model agreement maps, when the

363   dosage threshold is increased, the likelihood categories are affected. For this example, when the

364   dosage threshold is doubled, the distance the aircraft can travel while remaining in the 'likely'

365   category increased by a small amount while the distance travelled in the 'very likely' category

366   reduced (compare Figures 4(a) and (b) at the location of the westbound aircraft). This small

367   difference suggests that an operator may make a similar decision for both dosage thresholds for

368   this particular scenario. However, for a different air-route or eruption scenario a change in the

369   dosage threshold may have more of an effect on the likelihood boundaries.

370   Displaying model agreement as maps and along air routes provides aviation stakeholders

371   with a new method for displaying ensemble-based ash concentration and dosage information.

372   While this approach has been demonstrated for the JFK–LHR route, operators could apply the

373   same analysis to different or multiple flight tracks. The main advantage in displaying the data

374   this way is that decision-makers are provided with information about the confidence of the model

375   forecasts, which may improve flight-planning procedures.

376   **6. Risk maps and routes**

377   While the concept of model agreement is useful in that it can be used to indicate the likelihood of

378   a given impact (e.g. ash concentration and dosage) at a certain flight level and time, multiple

379   figures must be generated for varying thresholds of interest and may prevent an operator from

380   making a fast decision due to information overload. A risk-based approach has been shown to

381   reduce this issue for other hazards by condensing the ensemble information into a single map

382   (e.g. Neal *et al.*, 2014); thereby permitting multi-layered information in operational settings and

383   providing the users with the relevant information needed to make a decision.

384   6.1.   Ash concentration risk matrix

385   To construct a risk matrix both the impact and likelihood of the hazard must be combined

386   (shown schematically in Figure 5(a)). For the ash concentration risk matrix, the impact was

387   defined based on the following ash concentration (C) ranges (in mg m^{-3}): $0.2 < C \leq 2$, $2 < C <$

388   4 and $C \geq 4$. For the likelihood ranges, the same ranges in Section 5 were used: 0–10 % (less

389   likely), 10–90 % (likely) and 90–100 % (very likely); resulting in a 3 by 3 matrix (Figure 5(b)).

390   The boxes in the risk matrix each correspond to a different combination of impact and

391   likelihood. Following the approach of Neal *et al.* (2014), each box was assigned a colour using a

392   three-colour warning system (yellow, amber and red). The colours then correspond to a decision

393   to be made or action to be taken by the stakeholder. For example, if it is very likely (90–100%)

394   that the peak concentration will be low (0.2–2 mg m^{-3}) the risk level is shown in the top left box

395   of the ash concentration risk matrix (Figure 5(b)). The decision of a flight-planner in this

396   situation might be to allow the aircraft to fly its scheduled route and continue to check updated

397   forecasts. On the other hand, if it is very likely (90–100%) that the peak concentration will be

398   high ($\geq$ 4 mg m^{-3}) the risk level is shown in the top right box of the matrix. In this situation a

399   different action might be taken such as re-routing the aircraft. To illustrate how the risk matrix

400   might be used to make fast and robust decisions, the following example actions were assigned to

401   each colour warning (Figure 5(c)):

402   1) Yellow = Schedule route; check updated forecasts

403   2) Amber = Load more fuel; check updated forecasts; perform engine checks

404   3) Red = Consider alternative routes

405   Figures 6(a) and (b) show risk maps in the horizontal and vertical, respectively, for the same

406   valid meteorological time and altitude shown in Figure 3. Note that at each location on the risk

407   maps the colour warning corresponding to the maximum risk level is shown. For example, in a

408   location where the likelihood of the ash concentration exceeding 4 mg m^{-3} is less likely (i.e. an

409   amber warning) and the likelihood of the ash concentration being 0.2–2 mg m^{-3} is likely (yellow

410   warning), the latter is ignored in favour of the higher risk level. The horizontal risk map (Figure

411   6(a)) shows that amber and red warnings would be issued for airspace over the western part of

412   the British Isles while the areas between Iceland and the British Isles and over large parts of the

413 North Atlantic would be issued with red (high risk) warnings. In this situation, the decision for

414 aircraft planning routes over the amber regions of the risk map could be to load more fuel and

415 perform engine checks. Figure 6(b) shows that aircraft flying the time-optimal eastbound and

416 westbound routes between JFK and LHR at cruise altitude (FL350–FL550) would fly through

417 high risk regions; this means that alternative routes should be considered.

418   The risk-based approach to ash concentrations demonstrates how the four maps of Figure 3

419 can be condensed into one single figure, which can be used to make fast decisions and overcome

420 the issue of information overload for operators. It can also be used to see why each warning is

421 issued by illustrating which box in the risk matrix a particular location of interest corresponds to.

422 For example, the location annotated with a '+' within the amber region southwest of the British

423 Isles in Figures 7(a) and (b) corresponds to the bottom right box in the ash concentration risk

424 matrix. This means that $\leq$ 10% of the ensemble member simulations resulted in ash

425 concentrations greater than or equal to 4 mg m^{-3} at this location. The risk-based approach allows

426 for multiple layers of information about the ensemble of ash concentration forecasts. This is

427 useful, for example, in an operational environment where a simple colour warning may be

428 required for operators and regulators to take fast or immediate action. Intermediate information is

429 displayed by identifying a location in the risk matrix. This allows decision makers to distinguish

430 between, for example, amber warnings generated from a less likely ($\leq$ 10%), high impact ($\geq$ 4

431 mg m^{-3}) forecast and a likely (10–90%), medium impact (2–4 mg m^{-3}) forecast.

432 6.2.   Ash dosage risk matrix

433 The ash concentration risk, however, does not consider the potential risk of flying through low

434 ash concentrations for long durations of exposure or the potential to fly through high ash

435 concentrations for short durations of exposure without experiencing engine damage. To account

436 for these situations a dosage risk matrix was constructed (Figure 5(d)). The ash dosage, D,

437 impact was defined by the following ash dosage boundaries (in g m^{-3} s): $1.44 < D \leq 14.4$,

438 $14.4 < D < 28.8$ and $D \geq 28.8$ and the likelihood ranges were the same as those used for the

439 ash concentration risk matrix.

440 Figure 7(a) shows the along-route dosage risk corresponding to the dosage risk matrix

441 described above. Visualising the dosage risk along the route shows that an aircraft flying from

442 JFK to LHR return is predicted to encounter a region of high risk towards the end of the

443 eastbound section of the flight. In this case, a flight-planner may decide to 'consider alternative

444 routes' for the aircraft based on the red colour warning (Figure 5(c)).

445 This method can also be adapted so that both along-route dosage and peak concentration risk

446 are taken into account (Figure 7(b)). In this approach, the risk level corresponding to the higher

447 risk is selected. For example, in the section of the eastbound route between 40 ° W and 30 ° W

448 the peak concentration-based risk is higher than the dosage-based risk and so the route is

449 coloured according to the ash concentration-based risk level. This approach assumes that a high

450 peak concentration should be considered a high risk to the aircraft regardless of the duration of

451 exposure and is therefore more restrictive than using the dosage alone to determine the risk.

452 Current advice from Rolls-Royce is to perform engine checks if an aircraft is suspected to have

453 flown through peak concentrations greater than or equal to 4 mg m^{-3} and that dosages are a more

454 appropriate measure of engine susceptibility to volcanic ash (Clarkson and Simpson, 2017).

455 Figure 7(c) shows the full range (minimum and maximum) of possible along-route ash

456 concentrations and dosages generated from the ensemble for an aircraft flying through the thick

457 layer level (FL350–FL550) at T+30. The range of dosages produced by the ensemble was from

458 4.5–2000 g m^{-3} s (median of 160 g m^{-3} s) and the range of peak ash concentrations was from 0–

459   670 mg m^{-3} (ensemble median maximum of 38 mg m^{-3}). Analysis of the probability density

460   functions (PDFs) of the maxima of the along-route ash concentration and dosage shows that

461   these variables follow lognormal distributions (Figures 8(a), (b)). The along-route ash

462   concentration and dosage ensemble maxima (upper bounds of the shaded regions in Figure 7(c))

463   are therefore representative of rarely occurring extreme values. The occurrence of extreme

464   values in the ensemble, however, does not preclude the use of a risk matrix. To understand how

465   the risk warning is determined from the distribution of the ensemble, these data can be

466   represented by 'risk PDFs' (Figures 8(c), (d)) using ash concentration and dosage risk matrices.

467   Here the elements of the risk matrix are assigned numerical values (1–9) and the highest risk

468   value intersected by the distribution (re-binned according to the risk matrix impact boundaries)

469   determines the risk level. This approach has recently been suggested for a probabilistic, multi-

470   level wildfire warning system in Chile (Dacre *et al.*, 2018). An alternative, less conservative,

471   approach could be to use the mean or modal risk level. Figures 8(c) and (d) show that while

472   extreme values are present in the ensemble, the majority (> 90%) of the along-route ash

473   concentration and dosage maxima also exceed the maximum impact boundaries of the risk

474   matrices (defined in Sections 6.1 and 6.2). Therefore, one could be confident in a red risk

475   warning issued for the maximum ash concentration and dosage encountered along a return route

476   from JFK-LHR at FL350–FL550 and T+30. The advantage of this third layer of information is

477   that the forecaster can identify when the risk warning is due to outliers (i.e. a small number of

478   ensemble members predicting a high impact) and when the risk warning is confident (i.e. all

479   members predicting the same impact). Thus, even though the LHS dispersion model ensemble

480   members spanned several orders of magnitude in both the along-flight ash concentration and

481 dosage, the risk-based approach can still be used by flight-planners to make fast and robust

482 decisions.

483 **7. Discussion and conclusions**

484 The methodology described in this paper has been developed to show how a dispersion

485 model ensemble can be used to make fast and robust decisions during a hypothetical Icelandic

486 eruption scenario. The ability to make fast decisions, however, is contingent upon the forecast

487 service organisation having the computer resources necessary to conduct an ensemble forecast in

488 a short period of time. The method was applied to both volcanic ash concentrations and dosages.

489 To permit dosage calculations, aircraft routing software was used to generate time-optimal

490 eastbound and westbound trans-Atlantic flights from New York to London through a simulated

491 ash cloud over the North Atlantic.

492 To characterise the likelihood of certain ash concentration and dosage thresholds, the

493 concept of model agreement was used. Model agreement values rely on setting ash concentration

494 and dosage thresholds and were shown to be useful in visualising model confidence. Comparison

495 of the control run and the model agreement maps highlighted the importance of quantifying the

496 uncertainty in a deterministic forecast with an ensemble. In an operational context, these maps

497 could be used to plan flight paths closer to the ash cloud boundary in regions where model

498 confidence (agreement) is high than in regions where model confidence is low. This method is an

499 improvement to the subjective approach where the decision-maker infers their own uncertainty

500 by drawing a buffer (typically of uniform distance) around the deterministic ash cloud boundary

501 to indicate their perceived confidence in an ash concentration forecast (e.g. Mulder *et al.*, 2017).

502   To address the issue of information overload, risk matrices for both ash concentration and

503 dosage were constructed. These were used to demonstrate how fast decisions can be made when

504 taking uncertainty information into consideration. The risk matrix relies upon two key choices:

505 the choice of the likelihood boundaries and the choice of the impact (dosage and/or ash

506 concentration) boundaries. The choice of the likelihood and impact boundaries shown here were

507 based on discussions with aviation stakeholders and illustrate how this method can be

508 implemented. In an operational setting, these boundaries would be set prior to an eruption by the

509 user to reflect their risk appetite. One of the key advantages of this approach is that it allows the

510 user to make decisions even when faced with large sources of uncertainty in the model forecasts.

511 Additionally, visualising the dosage risk along the aircraft's route may be useful on an airline

512 operator fleet-scale where multiple risk routes are viewed on the same map.

513   The risk-based approach also encompasses varying levels of complexity. As shown with

514 the amber region example, an aircraft pilot may just require a colour warning to respond to the

515 hazard, while a dispersion modelling expert can query further to see what combination of

516 likelihood and impact caused the colour warning. A third step can be taken by looking at risk

517 probability density functions to identify when the risk warning is a result of outliers in the

518 ensemble and when the risk warning is confident. To effectively communicate this approach to

519 aviation stakeholders, the Volcanic Dosage And Risk Tool (VDART) has been developed

520 (accessible at http://www.met.reading.ac.uk/ash-dosage). The VDART interface has been

521 designed as a demonstration tool to illustrate how probabilistic forecasts of ash concentration and

522 dosage risk can be used to make fast and robust decisions. The web-tool was developed in

523 collaboration and consultation with aviation industry regulators, operators, engine manufacturers

524   and the UK Met Office and takes advantage of interactive data visualisation to communicate

525   uncertainty information.

526   Finally, this approach could potentially be applied to historical eruptions or extended to

527   other aviation hazards such as SO_2 and desert dust dosages or meteorological hazards such as

528   aircraft icing and clear-air turbulence. In cases where the model parameters are well constrained,

529   the ensemble could also be used for post-analysis when an engine manufacturer or airline

530   operator is trying to diagnose the likely range of dosages their engines have been exposed to.

531   **Acknowledgements**

546   Advisory Group (VASAG) are also acknowledged for their constructive comments on the web-

547   tool. Finally, two anonymous reviewers are thanked for their comments which led to significant

548   improvements to the manuscript. NAME simulation output presented in this paper is available on

549   the   University   of   Reading   Research   Data   Archive   (accessible   at

550   http://dx.doi.org/10.17864/1947.148).

551

552   **References**

553   Airbus 2017. *Airbus Global Market Forecast 2017–2036 "Growing horizons."* Airbus SAS:

554   Blagnac, France. http://www.airbus.com/content/dam/corporate-

555   topics/publications/backgrounders/Airbus_Global_Market_Forecast_2017-

556   2036_Growing_Horizons_full_book.pdf (accessed 17 November 2017).

557   Brown A, Milton S, Cullen M, Golding B, Mitchell J, Shelly A 2012. Unified modeling and

558   prediction of weather and climate: A 25-year journey. *B. Am. Meteorol. Soc.* **93**:1865–1877.

559   Buizza R, Palmer TN 1995. The Singular-Vector Structure of the Atmospheric Global

560   Circulation. *J. Atmos. Sci.* **52**:1434–1456.

561   Buizza R, Houtekamer PL, Toth Z, Pellerin G, Wei MZ, Zhu YJ 2005. A comparison of the

562   ECMWF, MSC, and NCEP global ensemble prediction systems. *Mon. Weather Rev.*

563   **133**:1076–1097.

564   Buizza R, Miller M, Palmer TN 1999. Stochastic representation of model uncertainties in the

565   ECMWF Ensemble Prediction System. *Q. J. R. Meteorol. Soc.* **125**:2887–2908.

566   CAA 2017. *CAP1236: Guidance regarding flight operations in the vicinity of volcanic ash.* Civil

567   Aviation Authority: Aviation House, Gatwick Airport South, UK.

568   http://publicapps.caa.co.uk/docs/33/CAP%201236%20FEB17.pdf (accessed 17 November

569   2017).

570   Casadevall TJ 1994. *Volcanic Ash and Aviation Safety: Proceedings of the First International*

571   *Symposium on Volcanic Ash and Aviation Safety*. U.S. Geol. Surv. Bull. 2047.

572   Christmann C, Nunes RR, Schmitt AR, Guffanti M 2017. Flying into Volcanic Ash Clouds: An

573   Evaluation of Hazard Potential. *Science and Technology Organization (STO) - Meeting*

574   *Proceedings Paper* **MP-AVT-272-KN3**:1–18.

575   Clarkson RJ, Simpson H 2017. Maximising Airspace Use During Volcanic Eruptions: Matching

576   Engine Durability against Ash Cloud Occurrence. *Science and Technology Organization*

577   *(STO) - Meeting Proceedings Paper* **MP-AVT-272-17**:1–20.

578   Clarkson RJ, Majewicz EJE, Mack P 2016. A re-evaluation of the 2010 quantitative

579   understanding of the effects volcanic ash has on gas turbine engines. *Proc. Inst. Mech. Eng.*

580   *G J. Aerosp. Eng.* **230**:2274–2291.

581   Cullen MJP 1993. The unified forecast/climate model. *Met. Mag.* **122**:81–94.

582   Dacre HF, Harvey NJ 2018. Characterising the atmospheric conditions leading to large error

583   growth in volcanic ash cloud forecasts. *Submitted to J. Appl. Meteorol. Climatol.*

584   Dacre HF, Grant ALM, Hogan RJ, Belcher SE, Thomson DJ, Devenish BJ, Marenco F, Hort

585   MC, Haywood JM, Ansmann A, Mattis I, Clarisse L 2011. Evaluating the structure and

586   magnitude of the ash plume during the initial phase of the 2010 Eyjafjallajökull eruption

587   using lidar observations and NAME simulations. *J. Geophys. Res.* **116**:D00U03.

588   Dacre HF, Grant ALM, Johnson BT 2013. Aircraft observations and model simulations of

589   concentration and particle size distribution in the Eyjafjallajökull volcanic ash cloud. *Atmos.*

590   *Chem. Phys.* **13**:1277–1291.

591 Dacre HF, Grant ALM, Harvey NJ, Thomson DJ, Webster HN, Marenco F 2015. Volcanic ash

592   layer depth: Processes and mechanisms. *Geophys. Res. Lett.* **42**:637–645.

593 Dacre HF, Crawford BR, Charlton-Perez AJ, Lopez-Saldana G, Griffiths GH, Vicencio Veloso J

594   2018. Chilean wildfires: Probabilistic prediction, emergency response and public

595   communication. *B. Am. Meteorol. Soc.* BAMS–D–17–0111.1.

596 Devenish BJ, Francis PN, Johnson BT, Sparks RSJ, Thomson DJ 2012. Sensitivity analysis of

597   dispersion modeling of volcanic ash from Eyjafjallajökull in May 2010. *J. Geophys. Res.*

598   *Atmos.* **117**:D00U21.

599 Folch A 2012. A review of tephra transport and dispersal models: Evolution, current status, and

600   future perspectives. *J. Volcanol. Geoth. Res.* **235-236**:96–115.

601 Gneiting T, Raftery AE 2005. Weather forecasting with ensemble methods. *Science* **310**:248–

602   249.

603 Guffanti M, Tupper A 2015. Volcanic Ash Hazards and Aviation Risk. In: *Volcanic Hazards,*

604   *Risks and Disasters*. Elsevier, 87–108.

605 Guffanti M, Casadevall TJ, Budding K 2010. Encounters of aircraft with volcanic ash clouds; a

606   compilation of known incidents, 1953-2009. *U.S. Geol. Surv. Data Ser.* **545**:1–16.

607 Harvey NJ, Huntley N, Dacre HF, Goldstein M, Thomson D, Webster H 2018. Multi-level

608   emulation of a volcanic ash transport and dispersion model to quantify sensitivity to

609   uncertain parameters. *Nat. Hazards Earth Syst. Sci.* **18**:41–63.

610 ICAO 2007. *Doc 9691 AN/954: Manual on Volcanic Ash, Radioactive Material and Toxic*

611   *Chemical Clouds, Second Edition – 2007.* International Civil Aviation Organization:

612   Montréal, Quebec, Canada. https://skybrary.aero/bookshelf/books/2997.pdf (accessed 5

613   February 2018).

614   ICAO 2016. *Volcanic Ash Contingency Plan, European and North Atlantic Regions. EUR Doc.*

615   *019, NAT Doc. 006, Part II. Edition 2.0.0 – July 2016.* International Civil Aviation

616   Organization: Neuilly-sur-Seine, France.

617   https://www.icao.int/EURNAT/EUR%20and%20NAT%20Documents/EUR+NAT%20VAC

618   P.pdf (accessed 26 February 2018).

619   Iman RL, Conover WJ 1980. Small sample sensitivity analysis techniques for computer models,

620   with an application to risk assessment. *Commun. Stat. Part A* **9**:1749–1842.

621   Irvine EA, Hoskins BJ, Shine KP, Lunnon RW, Froemming C 2013. Characterizing North

622   Atlantic weather patterns for climate-optimal aircraft routing. *Meteorol. Appl.* **20**:80–93.

623   Irvine EA, Shine KP, Stringer MA 2016. What are the implications of climate change for trans-

624   Atlantic aircraft routing and flight time? *Transp. Res. D: Transp. and Environ.* **47**:44–53.

625   Jones A, Thomson D, Hort M, Devenish B 2007. The U.K. Met Office's Next-Generation

626   Atmospheric Dispersion Model, NAME III. In: *Air Pollution Modeling and Its Application*

627   *XVII*. Boston, MA: Springer US, 580–589.

628   Kristiansen NI, Prata AJ, Stohl A 2015. Stratospheric volcanic ash emissions from the 13

629   February 2014 Kelut eruption. *Geophys. Res. Lett.* **42**:588–596.

630   Lawrence BN, Bennett VL, Churchill J, Juckes M, Kershaw P, Oliver P, Pritchard M, Stephens

631   A 2012. The JASMIN super-data-cluster. *arXiv:1204.3553 [cs.DC]*.

632   Lunnon RW, Marklow AD 1992. Optimization of Time Saving in Navigation Through an Area

633   of Variable Flow. *J. Navig.* **45**:384–399.

634   Mastin LG, Guffanti M, Servranckx R, Webley P, Barsotti S, Dean K, Durant A, Ewert JW, Neri

635   A, Rose WI, Schneider D, Siebert L, Stunder B, Swanson G, Tupper A, Volentik A,

636   Waythomas CF 2009. A multidisciplinary effort to assign realistic source parameters to

637   models of volcanic ash-cloud transport and dispersion during eruptions. *J. Volcanol. Geoth.*

638   *Res.* **186**:10–21.

639   Millington SC, Saunders RW, Francis PN, Webster HN 2012. Simulated volcanic ash imagery:

640   A method to compare NAME ash concentration forecasts with SEVIRI imagery for the

641   Eyjafjallajkull eruption in 2010. *J. Geophys. Res. Atmos.* **117**:D00U17.

642   Mulder KJ, Lickiss M, Harvey N, Black A, Charlton-Perez A, Dacre H, McCloy R 2017.

643   Visualizing Volcanic Ash Forecasts: Scientist and Stakeholder Decisions Using Different

644   Graphical Representations and Conflicting Forecasts. *Wea. Climate Soc.* **9**:333–348.

645   Neal RA, Boyle P, Grahame N, Mylne K, Sharpe M 2014. Ensemble based first guess support

646   towards a risk-based severe weather warning service. *Meteorol. Appl.* **21**:563–577.

647   Palmer TN 2002. The economic value of ensemble forecasts as a tool for risk assessment: From

648   days to decades. *Q. J. R. Meteorol. Soc.* **128**:747–774.

649   Peterson RA, Dean KG 2007. Forecasting exposure to volcanic ash based on ash dispersion

650   modeling. *J. Volcanol. Geoth. Res.* **170**:230–246.

651   Prata AJ, Prata AT 2012. Eyjafjallajökull volcanic ash concentrations determined using Spin

652   Enhanced Visible and Infrared Imager measurements. *J. Geophys. Res. Atmos.* **117**:D00U23.

653   Prata AJ, Tupper A 2009. Aviation hazards from volcanoes: The state of the science. *Nat.*

654   *Hazards* **51**:239–244.

655   Prata AJ, Kristiansen N, Thomas HE, Stohl A 2018. Ash metrics for European and trans-Atlantic

656   air routes during the Eyjafjallajökull eruption 14 April-23 May, 2010. *J. Geophys. Res.*

657   *Atmos.*

658   Rolls-Royce 2017. *All RB211 and Trent Engines - Volcanic Ash Limits Guidance.* Rolls-Royce

659   plc: Derby, UK. https://www.wmo.int/aemp/sites/default/files/VA_Limits_Guidance_Rolls-

660   Royce.pdf (accessed 17 November 2017).

661   Stohl A, Prata AJ, Eckhardt S, Clarisse L, Durant A, Henne S, Kristiansen NI, Minikin A,

662   Schumann U, Seibert P, Stebel K, Thomas HE, Thorsteinsson T, Tørseth K, Weinzierl B

663   2011. Determination of time- and height-resolved volcanic ash emissions and their use for

664   quantitative ash dispersion modeling: the 2010 Eyjafjallajökull eruption. *Atmos. Chem. Phys.*

665   **11**:4333–4351.

666   Webster HN, Thomson DJ, Johnson BT, Heard IPC, Turnbull K, Marenco F, Kristiansen NI,

667   Dorsey J, Minikin A, Weinzierl B, Schumann U, Sparks RSJ, Loughlin SC, Hort MC,

668   Leadbetter SJ, Devenish BJ, Manning AJ, Witham CS, Haywood JM, Golding BW 2012.

669   Operational prediction of ash concentrations in the distal volcanic cloud from the 2010

670   Eyjafjallajökull eruption. *J. Geophys. Res. Atmos.* **117**:D00U08.

671   Witham CS, Webster HN, Hort MC, Jones A, Thomson D 2012. Modelling concentrations of

672   volcanic ash encountered by aircraft in past eruptions. *Atmos. Environ.* **48**:219–229.

673   Witham CS, Hort MC, Thomson D, Leadbetter SJ, Devenish BJ, Webster HN, Beckett FM 2016.

674   The current volcanic ash modelling set-up at the London VAAC. *Met Office Technical*

675   *Summary (v1.3)*:1–9.

676   Wylie S, Bucknell A, Forsyth P, McGilvray M, Gillespie DRH 2017. Reduction in Flow

677   Parameter Resulting From Volcanic Ash Deposition in Engine Representative Cooling

678   Passages. *J. Turbomach.* **139**:031008.

680

Tables

Parameter	Control value	Sampling range
Plume height (km)	15	13 to 17
Mass eruption rate factor	1	1/3 to 3
Source duration (h)	16	6 to 26
Source timing (UTC)	0300 1 Jan 2017	0300 to 1300 1 Jan 2017
Distal fine ash fraction (%)	5	1 to 10
Horizontal (vertical) Lagrangian timescale (τ) for free tropospheric turbulence (s)	300 (100)	100 to 900 (33.33 to 300)
Standard deviation (σ) of horizontal (vertical) velocity for free tropospheric turbulence (m s^{-1})	0.25 (0.10)	0.0025 to 2.5 (0.001 to 1)
Standard deviation (σ) of horizontal velocity for unresolved mesoscale motions (m s^{-1})	0.8	0.27 to 1.74
Meteorological fields	MetUM analysis	ECMWF members 0 to 19

Table 1. Control run parameters selected for Latin Hypercube Sampling.

684   **Figures**
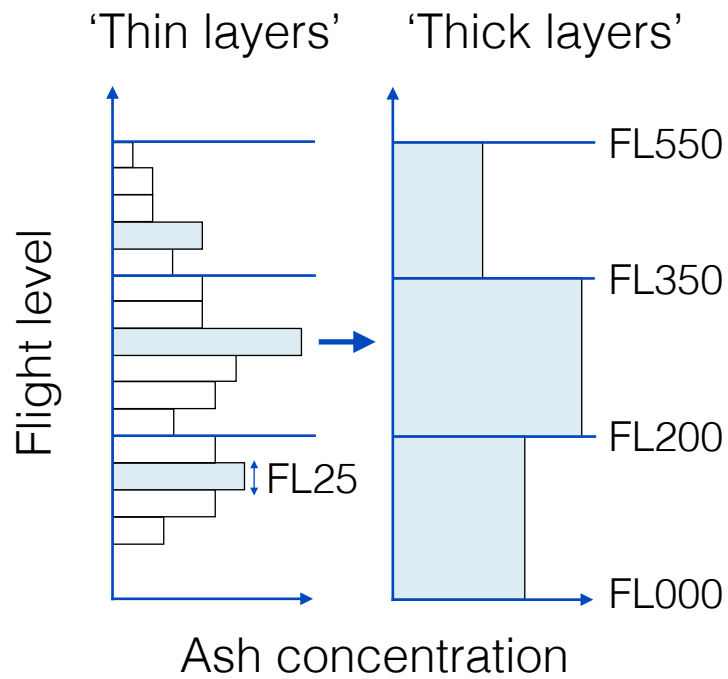
685

686   Figure 1. Schematic showing the difference between the thin layer and thick layer LVAAC setup of NAME.

687
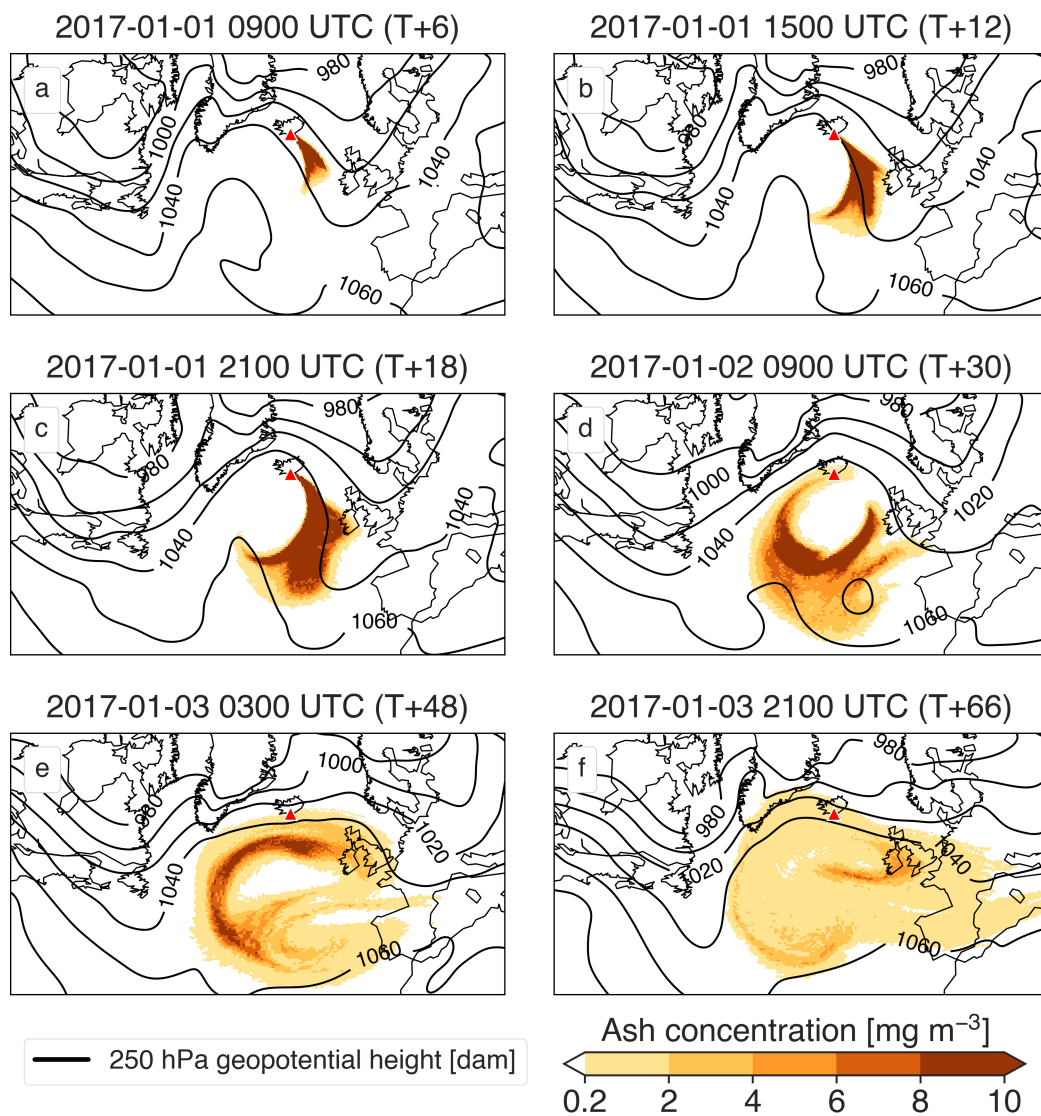
Figure 2. Ash concentrations for the control run simulation for the Katla (indicated by the red triangle) eruption
scenario with 250 hPa geopotential height contours overlaid. The control run start time is 0300 UTC on 1 January
2017. Concentrations have been post-processed to produce the LVAAC's thick layer product from FL350–FL550.
(a) 6, (b) 12, (c) 18, (d) 30, (e) 48, (f) 66 hours after eruption.
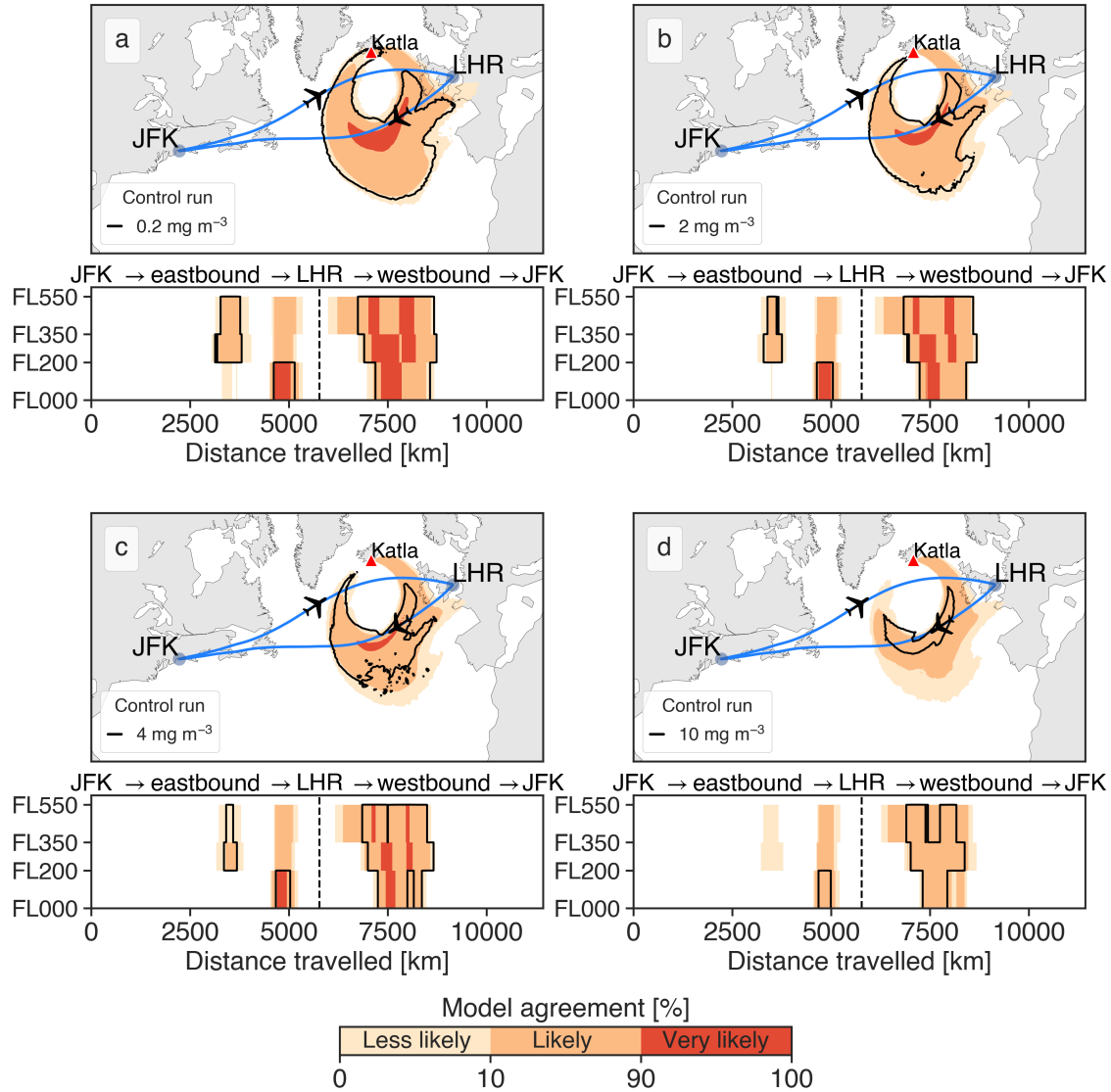
Figure 3. Percentage of ensemble members at T+30 that resulted in ash concentrations above (a) 0.2 mg m^{-3}, (b) 2 mg m^{-3}, (c) 4 mg m^{-3} and (d) 10 mg m^{-3}. Each panel shows the geographic model agreement and the relevant ash concentration contour for the control run (black line) at the FL350–FL550 thick layer level (top) and the vertical cross-section of model agreement and the relevant ash concentration contour along the JFK–LHR and LHR–JFK time-optimal routes (bottom).
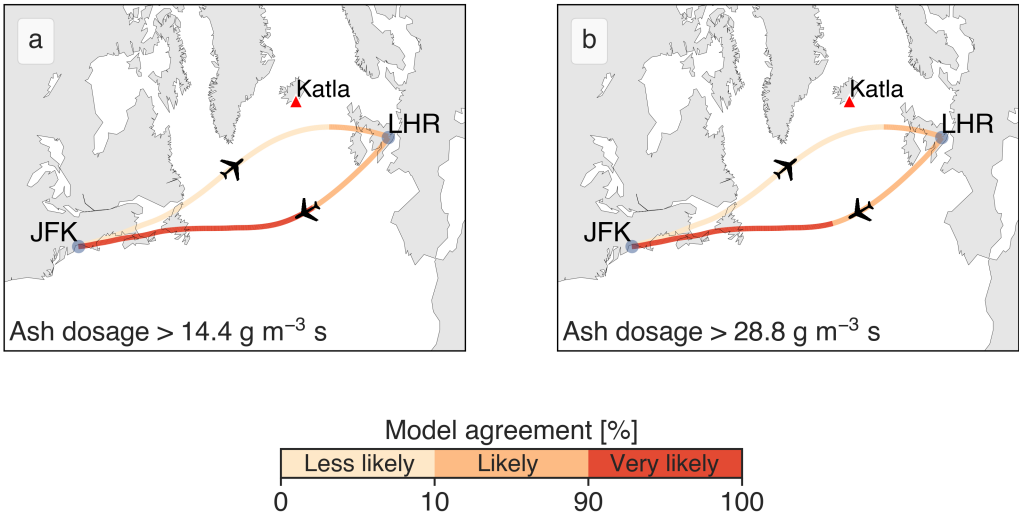
Figure 4. Percentage of ensemble members that resulted in ash dosages above (a) 14.4 g m^{-3} s and (b) 28.8 g m^{-3} s. Percentages have been calculated along the time-optimal eastbound and westbound flight routes between JFK and LHR at T+30 for the FL350–FL550 thick layer level.
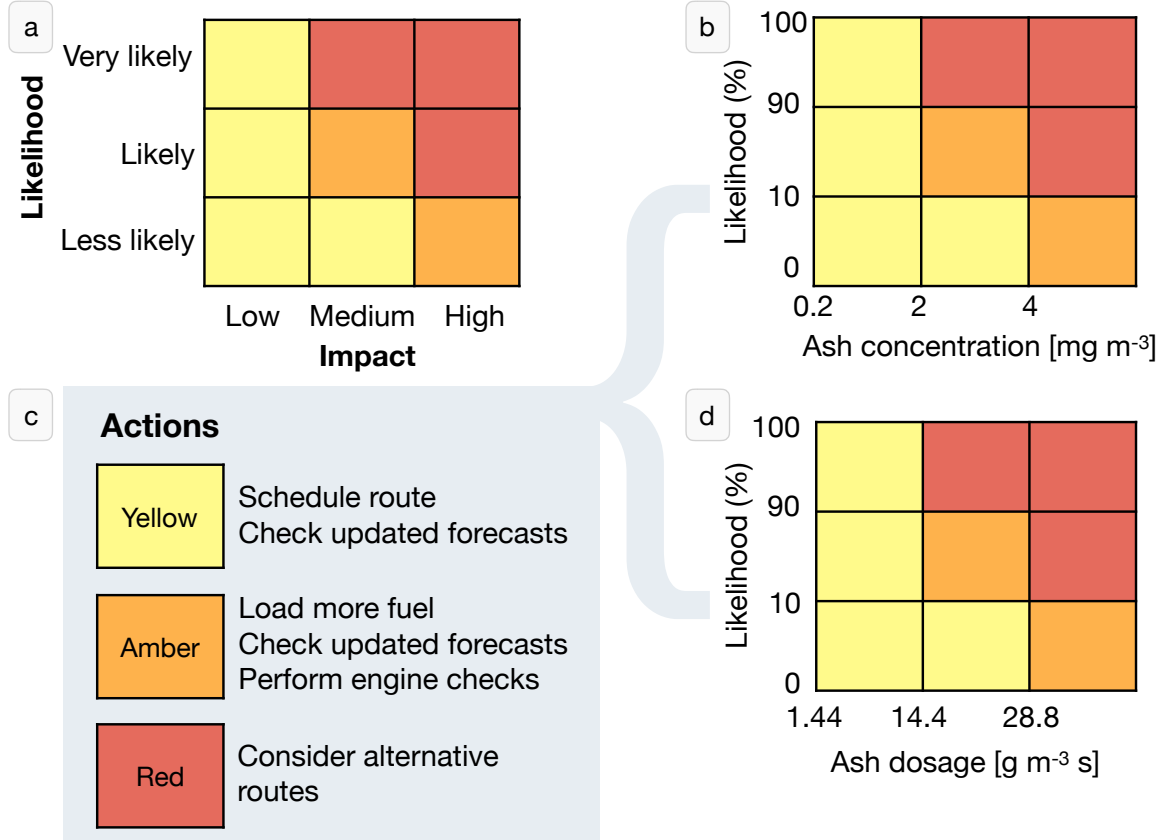
Risk = Impact x Likelihood

703

Figure 5. Schematic showing (a) a generic risk matrix, (b) how the ash concentration risk matrix was constructed, (c) example actions that could be taken by a decision-maker in response to a yellow, amber or red warning and (d) how the ash dosage risk matrix was constructed.
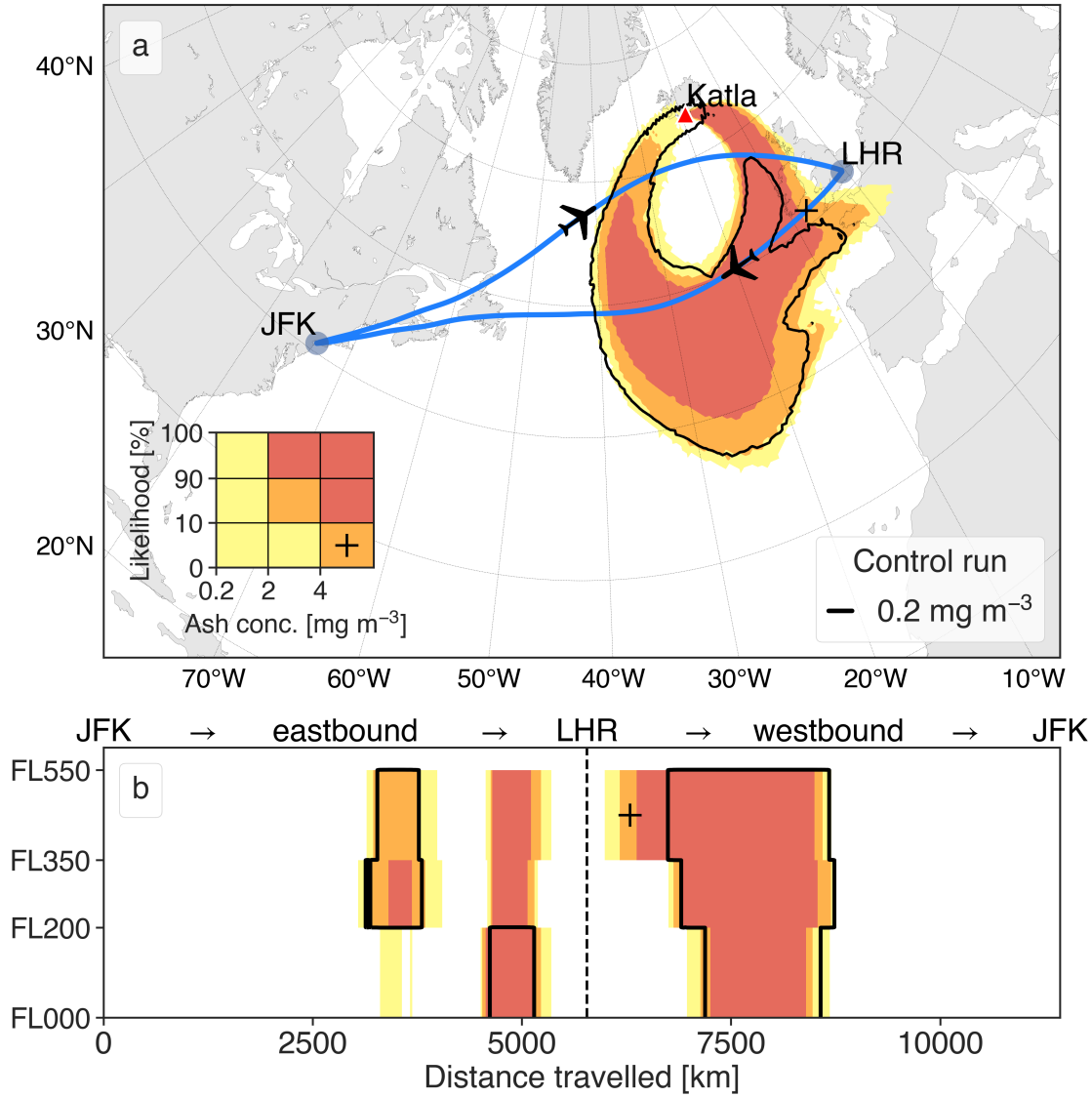
Figure 6. (a) Horizontal ash concentration risk map for the thick layer level (FL350–FL550) at T+30. (b) Vertical risk maps for each thick layer corresponding to the return JFK–LHR route (plotted on (a)) at T+30. The '+' annotated on the risk matrix (inset of (a)) corresponds to the risk level at the location of the '+' on (a) and (b).
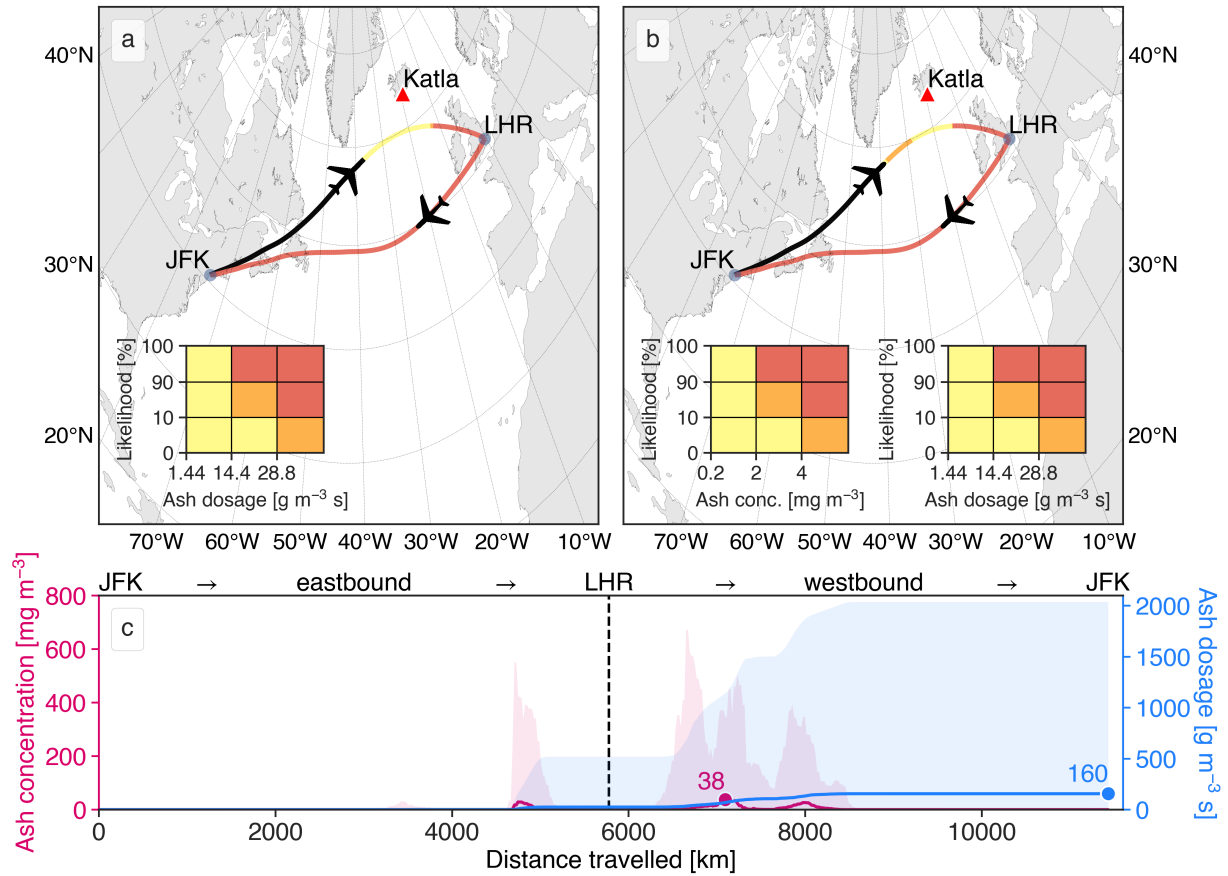
711

Figure 7. (a) Dosage risk for the New York (JFK) to London (LHR) trans-Atlantic air-route at T+30 and thick layer

level FL350–FL550. (b) Dosage and ash concentration risk for the same route in (a). (c) Along-route ash

concentration and dosage. Values annotated are the ensemble median maximum values correct to two significant

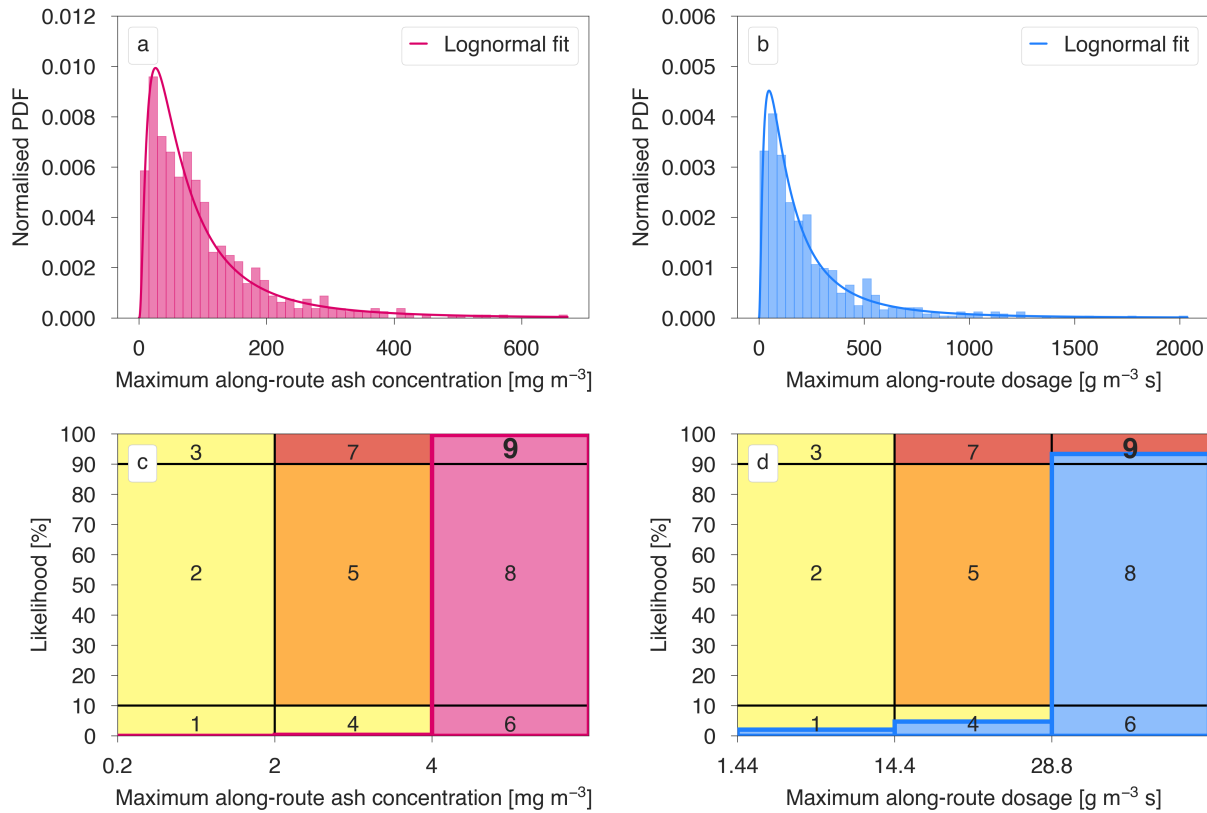figures; shaded regions correspond to minimum and maximum of the ash concentration and dosage.

716

Figure 8. Normalised probability density functions (PDFs) of the maxima of the (a) along-route ash concentration and (b) along-route dosage for the return air-route from New York (JFK) to London (LHR) at T+30 and thick layer level FL350–FL550 (lines plotted over each histogram indicate a Lognormal distribution fit). The 'risk PDFs' corresponding to the distributions shown in (a) and (b) are illustrated in (c) and (d), respectively. Note that the numerical values annotated on (c) and (d) indicate the risk level, with the risk issued shown in bold). The pink and blue histograms plotted over the risk matrix have been re-binned according to the impact boundaries shown in Figure 5.